AIAA JOURNAL
Vol. 35, No. 2, February 1997

Reynolds Stress Transport Equations in a Momentumless Wake: Experiments and Models

Thierry M. Faure*
École Centrale de Lyon, 69 131 Écully, France

The determination of the transfer terms in the Reynolds stress transport equations is an important issue in the improvement of closure models in turbulence. A part of these efforts is to provide accurate experimental information on each term of these equations and, particularly, on the pressure-strain term. The self-similar region of the momentumless wake of an axisymmetric, propeller-driven body is studied to enable the required balances of the Reynolds stress transport equations. The axial and azimuthal balances show that the flow is mainly dominated by convection. For the shear equations, there is a quasiequilibrium between production and pressure strain, except in the center of the wake. Comparisons are made between the experimentally determined distributions of pressure-strain terms and the corresponding distributions predicted by second-order closure models. The quasi-isotropic model and the isotropic production model do not predict well the amplitude of the pressure-strain term. Fu's model, calibrated for a strongly swirling recirculating jet, gives the best results in comparison with experimental data.

I. Introduction

REYNOLDS stress transport equations are important for understanding physical phenomena in a flow, mainly because of the wide use of second-order closure models in turbulent numerical codes. The aim of the present study is to investigate the momentumless axisymmetric wake of a propeller-driven body, where the drag of the body is completely canceled by the thrust created by the propulsion system. For this kind of flow, however, very few experimental data are available, and no Reynolds stress balances have been published. Note that these results are available for wall-bounded flows such as a manipulated boundary layer,[1] a wing/body junction,[2] and the flow around a surface mounted cube.[3] However, for nonbounded flows, these budgets are given only for plane jets,[4] axisymmetric jets,[5,6] and two-dimensional wakes.[7] We provide measurements of the balances for the self-similar region of a momentumless wake tested in a wind tunnel. For that wake, the flow is characterized by a mean azimuthal velocity, a component that does not exist in the case of a jet-driven body.[8,9] The experimental determination of these balances permits the radial evolution of the pressure-strain term to be obtained. A comparison between this term and the one given by classical second-order closure models is presented. Different expressions for this term, determined for shear flow with swirl[10,11] or without swirl[12] are tested.

II. Experimental Arrangements

The wake is generated by an axisymmetric, streamlined body, mounted in the working section of a wind tunnel (500 × 500 mm, 6 m long). The experimental freestream velocity can vary from 5 to 80 m/s with a uniformity of ±2% and a maximum turbulence intensity of 0.7%. The model has a diameter of 8 cm and a length of 50 cm (Fig. 1). It has an elliptical nose, a cylindrical middle section and a conical stern. The propulsion system consists of a three-blade marine type propeller with a diameter of 4 cm. The inside of the body is hollow and contains the motor (15,000-rpm maximum speed), which drives the propeller. An electronic system is available to control the rotation speed. A supporting device having a symmetrical NACA 66_1 012 profile with a chord of 10 cm and a maximum width of 1.2 cm was chosen to minimize aerodynamic perturbations around the body. Electrical wires for power supply and speed regulation are mounted inside this support. An alignment system permits the model to fit with the freestream flow. Once this adjustment is made, the angle between the wake axis and the tunnel axis was found to be less than 0.3 deg.

For a self-propelled body, the drag generated by the model equals the thrust created by the propulsion system. These quantities could be obtained by the measurement of the support force on the body. Unfortunately, a direct determination of this force was not available in this study. Thus, to bring about self-propulsion, a momentum balance was established for the model. To this effect, we had two parameters that were able to vary, the freestream velocity and the propeller rotation speed. The propeller rotation was fixed at its maximum value, and the freestream velocity was varied to make the drag equal to the thrust. In Fig. 2, the thrust minus drag balance is normalized by the upstream momentum flux and plotted vs the freestream velocity. The different quantities of this balance were measured with a five-hole pressure probe, which gave the mean velocity and pressure. Note that the probe generates a nonlinear averaging function in the estimate of pressure in a turbulent flow. As a consequence, it produces an uncertainty in the determination of the balance. Mean velocities have been checked

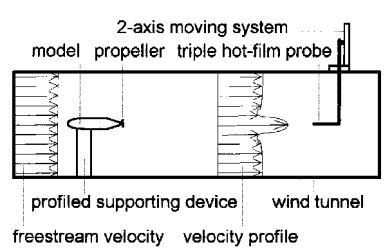

Fig. 1 Experimental setup.

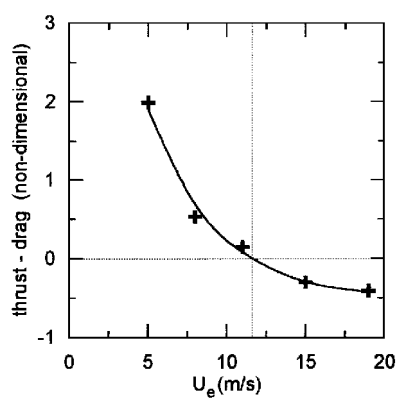

Fig. 2 Variation of the thrust–drag balance with the freestream velocity.

Received March 19, 1996; presented as Paper 96-2037 at the AIAA 27th Fluid Dynamics Conference, New Orleans, LA, June 17–20, 1996; revision received Sept. 16, 1996; accepted for publication Oct. 20, 1996; also published in *AIAA Journal on Disc*, Volume 2, Number 2.

*Postdoctoral Research Assistant, Laboratoire de Mécanique des Fluides et d'Acoustique, Unité Mixte de Recherche 5509, Centre National de la Recherche Scientifique. Member AIAA.

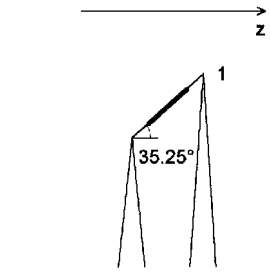

Side view (sensor 1)

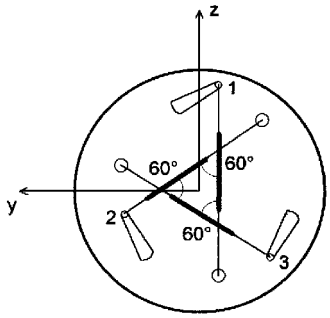

Front view

Fig. 3 Triple-sensor probe geometry.

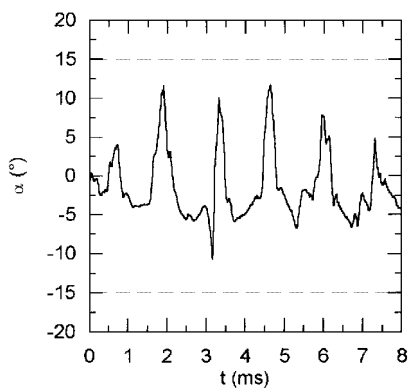

Fig. 4 Time sample of the angle α = arctan (V/U) for the maximum turbulence intensity point (x/D = 0.44 $r/r*$= 0.6).

with the hot-film measurements. Self-propulsion was realized with a freestream velocity of 11.6 $\pm$ 0.25 m/s; the uncertainty is due to the pressure estimate and the freestream velocity deviation. The corresponding Reynolds number based on the diameter of the body was $Re = 5.8 \times 10^4$.

The flow is three dimensional and turbulent; it is, therefore, necessary to use a directional probe that can measure both the mean and the fluctuating parts of the velocity. An automated triple hot-film anemometry system, which has been developed in the laboratory, gives all three components of instantaneous velocity. The probe is a Dantec 55R91 type, with the active lengths of the three sensors included into a sphere of diameter $d = 1.2$ mm. The smallest Kolmogorov microscale is $\eta = 0.4$ mm, which is in comparison with the measurement volume according to the relation $d \leq 3\_4\,\eta$ given by Wyngaard and Pao.[13] Each sensor is a nickel film deposited on a quartz cylinder, 70 μm in diameter. The three film supports are orthogonal and inserted into a sphere of 3 mm diameter (Fig. 3). This dimension corresponds to the Taylor scale of the structures encountered in the flow. Calibration of each sensor is performed in the unperturbed freestream. From calibration data, three King's laws are determined for each film. Then, the probe is carefully adjusted with the flow to use Jorgensen's geometric relations.

Figure 4 shows a time sample of the angle α between the radial and axial velocity components for the location in the wake where the flow is strongly marked by the blade passage influence and where the maximum turbulence intensity is measured. For this position, α reaches its maximum value. Note the peaks in the sample, distributed every 1.3 ms and linked with the periodic blade passage, which generates a rapid change in the velocity direction. Nevertheless, this angle remains inside the 15-deg acceptance cone, which is the limit for unambiguous velocity determination with a triple sensor probe.

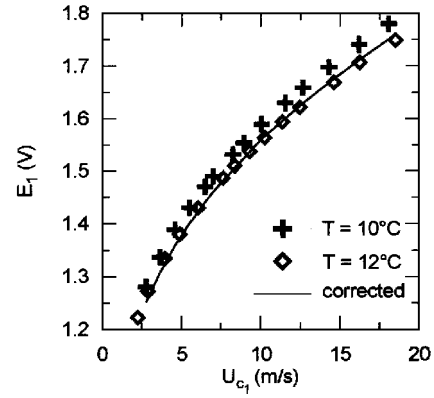

Fig. 5 Temperature drift effect on the calibration curve and its correction for hot-film number 1.

When an experiment is performed, a long time is necessary to move the probe after data acquisition at each point of measurement, leading to a long experimental time (typically, 4 h). As a consequence, the ambient temperature during measurements may change and can affect the data processing because the calibration curves can be modified with the temperature. Film aging or contamination problems may introduce similar effects in these curves. Thus, periodic verification is carried out during the acquisition procedure: the probe is placed in the freestream from time to time and a calibration point obtained for each film. As part of the signal processing, such points are used to update the calibration curve. Figure 5 shows two calibration curves (output voltage vs cooling velocity) for sensor 1 plotted for two ambient temperatures with a 2°C temperature drift. The solid line is the corrected curve for the calibration achieved for $T = 10$°C when it is used to process data acquired at temperature $T = 12$°C. The agreement between the corrected curve and the calibration curve performed at 12°C is very good because a deviation smaller than 0.94% is found. The films are operated as constant temperature anemometers at an overheat ratio of 0.8. The anemometer is a 3-channel TSI IFA 100 type including a conditioner unit for each channel. Output voltages from the anemometer are passed through buck and gain circuits. To avoid aliasing, the signal should be low-pass filtered at a cutoff frequency that is half the sampling frequency. The low-pass filters, which are identical for each conditioner unit, are third-order, $_$18-dB per octave, Sallen-Key type. The phase shifts introduced are identical; the cross spectra between the measured voltages delivered by each channel were checked that no phase deviation was detected. Then, the data are digitized with a 12-bit A/D converter. Three types of acquisition were necessary for a single point of measurement, to determine correctly the desired quantities: 1) a sampling frequency of 4 kHz, to measure the mean and the second-order moments of velocity components; 2) a sampling frequency of 7.5 kHz with a sample of at least 20 s to obtain the convergence of third-order moments; and 3) a sampling frequency of 50 kHz for a good estimate of spectra E_{ij} and an accurate evaluation of the dissipation function.

The data are stored on the hard disk of a 80386 PC computer for later processing. The various error sources all along the acquisition procedure are carefully identified (see Ref. 14). They are as follows.

1) The conditioning error is due to the buck and gain process of signal before treatment. In this study, the values delivered by the signal conditioning unit were checked, and do not generate any voltage deviation.

2) The digital error is due to signal sampling. This error is maximized in the case of no previous signal conditioning (gain = 1, buck = 0). In the present study, where the voltages were optimized before sampling, this error is found to be less than 0.04% and can be neglected.

3) The thermal response variation of the sensor is a potential error source in the processed velocity. Here, a temperature variation is corrected in the previously mentioned way, leading to a maximum deviation of 0.94%. If this procedure is not carried out, a variation of 2°C between the calibration temperature and the measurement temperature can induce errors of 12.5% in the mean velocity.

4) The signal treatment error is due to the inversion of the voltages delivered by the anemometer, into the velocity components. From the range of velocity processed in this study, the corresponding error is 0.33%.

5) The statistical treatment error is related to the moment of velocity measured. The average time has to be adjusted with the desired moment. Note that for velocity moments greater than one, this is the only important error source. In this work we found statistical errors of 0.43% for mean velocity, 1.4% for second moments, and 2.7% for triple moments.

Finally, the maximum global measurement errors were found to be 1.7% for mean velocity, 1.4% for second-order moments, and 2.7% for third-order moments.

III. Reynolds Stress Transport Equations

We consider a simplified expression for each Reynolds stress transport equation, using a boundary-layer approximation[15] that is based on an analysis of the order of magnitude for each term. This is justified because measurements are carried out in the self-similar part of the wake.[16] In Fig. 6, the turbulent kinetic energy $\overline{q^2} = 1/2(\overline{u^2} + \overline{v^2} + \overline{w^2})$, where u, v, and w are, respectively, the velocity fluctuations for the axial, radial, and azimuthal directions, is normalized by its local maximum value $\overline{q^2}_m(x/D)$. The radial coordinate is scaled with the radius of the wake $r*$ defined as the location at which the axial turbulence intensity had fallen to half of its maximum value. The same profile is found for any axial position, illustrating self-similarity of the turbulent flow in the far wake. Then, each Reynolds stress transport equation can be written as the balance,

$$C_{ij} = P_{ij} + T^1_{ij} + T^2_{ij} + \Pi_{ij} - \varepsilon_{ij} \tag{1}$$

where the terms denote convection C_{ij}, production P_{ij}, turbulent transfer T^1_{ij}, pressure transfer T^2_{ij}, pressure-strain Π_{ij}, and dissipation $-\varepsilon_{ij}$, respectively. Their general expressions in Cartesian coordinates are

$$C_{ij} = \bar{U}_k \frac{\partial \overline{u_i u_j}}{\partial x_k} \qquad P_{ij} = -\overline{u_i u_k}\frac{\partial \bar{U}_j}{\partial x_k} - \overline{u_j u_k}\frac{\partial \bar{U}_i}{\partial x_k}$$

$$T^1_{ij} = -\frac{\partial \overline{u_i u_j u_k}}{\partial x_k} \qquad T^2_{ij} = -\frac{\partial}{\partial x_k}\left(\overline{\frac{pu_i}{\rho}}\delta_{jk} + \overline{\frac{pu_j}{\rho}}\delta_k\right)$$

$$\Pi_{ij} = \overline{\frac{p}{\rho}\left(\frac{\partial u_i}{\partial x_j} + \frac{\partial u_j}{\partial x_i}\right)} \qquad \varepsilon_{ij} = 2\nu\overline{\frac{\partial u_i}{\partial x_k}\frac{\partial u_i}{\partial x_k}}$$

where δ_j is the Kronecker symbol. The subscripts denote the axes. Repeated dummy indices in a multiplication denote summation. In a wake, the molecular diffusion is neglected because there are no wall effects.

The method used to experimentally determine the Reynolds stress transport balances is similar to the one described by Browne et al.[17] Each term of the equation is measured except for the pressure transfer and pressure-strain terms, which are determined from the overall balance. The axial gradient, appearing on the convection term, is defined from the self-similar form

$$\overline{u_i u_j} = \overline{u_i u_j}_m (x/D) h_{ij}(r/r*)$$

where $\overline{u_i u_j}_m$ is the maximum value of $\overline{u_i u_j}$ at station x/D and $r/r*(x/D)$ is the radial similarity variable. Thus,

$$\frac{\partial \overline{u_i u_j}}{\partial x} = \left[\frac{\mathrm{d}\overline{u_i u_j}_m}{\mathrm{d}x}\left(\frac{x}{D}\right)h_{ij}\left(\frac{r}{r*}\right) - \overline{u_i u_j}_m\left(\frac{x}{D}\right)\frac{r}{r*^2}\frac{\mathrm{d}r*}{\mathrm{d}x}\left(\frac{x}{D}\right)\frac{\mathrm{d}h_{ij}}{\mathrm{d}(r/r*)}\left(\frac{r}{r*}\right)\right] \Big/ D$$

A least-square spline fit is first applied to the data on $h_{ij}(r/r*)$ before numerical differentiation yielding $\mathrm{d}h_{ij}/\mathrm{d}(r/r*)$. The radial derivatives of these quantities that appear in the production terms are obtained in a similar way. The three third-order moments of the turbulent transfer terms can be measured directly, thanks to the triple hot-film probe.

Dissipation of turbulent kinetic energy ε is determined by means of an isotropic formulation,

$$\varepsilon = 15\nu\overline{\left(\frac{\partial u}{\partial x}\right)^2}$$

The integration of the dissipation spectrum is preferred to avoid the influence of the energetic part of the spectrum in the estimate of the dissipation function

$$\varepsilon = 15\nu\int_0^\infty k_1^2 E_{11}(k_1)\,\mathrm{d}k_1$$

The reliability of this expression is good because the Reynolds number, based on the turbulent velocity and the Taylor scale, is around 140. In addition, Fig. 7 shows the comparison between the dissipation spectrum $k_1^2 E_{11}(k_1)$ and two spectra of the radial velocity determined in different ways: the first one is the measured spectrum $E_{22}(k_1)$ and the second one is calculated with the isotropic formulation from measurements of the spectrum of the axial velocity $E_{11}(k_1)$ (Ref. 18). We note that in the range of wave numbers where dissipation reaches its maximum, the agreement between the two spectra is good. The dissipation of the Reynolds stress transport equations ε_{ij} is determined from the dissipation of turbulent kinetic energy ε,

$$\varepsilon_{ij} = \tfrac{2}{3}\varepsilon\delta_{ij}$$

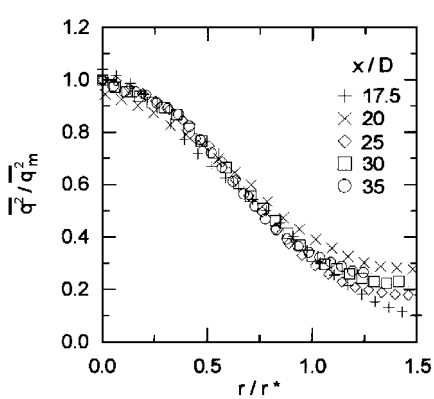

Fig. 6 Self-similar turbulent kinetic energy profile.

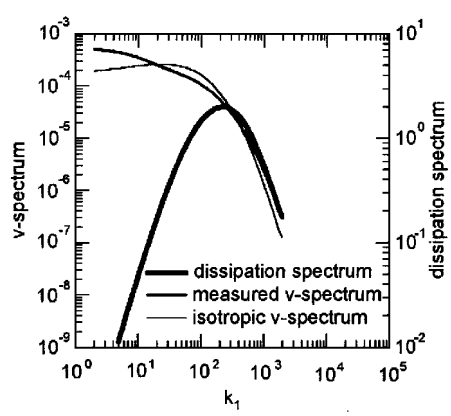

Fig. 7 Comparison between the dissipation spectrum and the measured and isotropic *v* spectra.

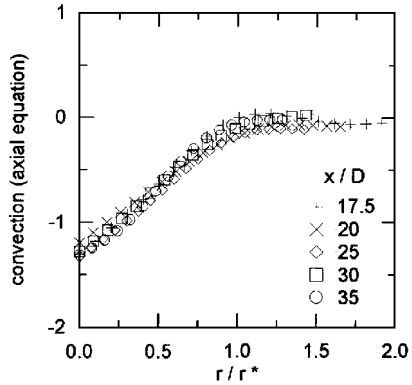

Fig. 8 Self-similar profile of convection for the axial Reynolds stress equation.

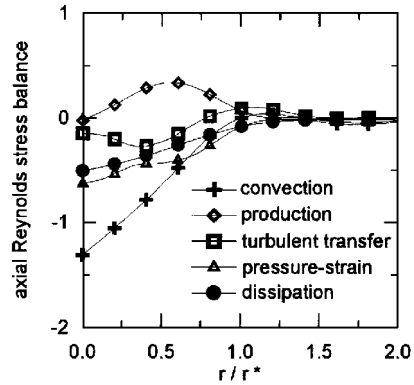

Fig. 9 Axial Reynolds stress balance.

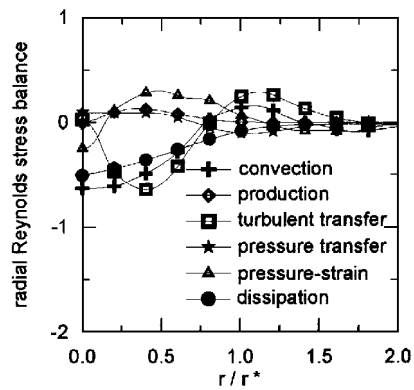

Fig. 10 Radial Reynolds stress balance.

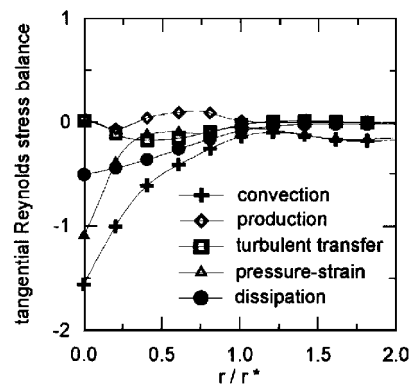

Fig. 11 Tangential Reynolds stress balance.

For the axial, radial, and tangential equations this term exists, and it vanishes in the shear stress equations.

All of the results presented are carried out in the self-similar far momentumless wake, for axial distances from the trailing edge of the propeller $x/D \geq 17.5$. Note that the balances are nondimensional and normalized by

$$\overline{q^2}^{\frac{3}{2}}/r*$$

Self-similarity is pointed out in the convection term for the axial Reynolds stress equation (Fig. 8), where the different symbols are associated to different axial locations in the wake. This self-similar behavior is also checked for the other terms and other equations.

The distributions of the axial, radial, and tangential Reynolds stress transport equations and the axial–radial and radial–tangential shear transport equations are given. For the axial and tangential equations, the pressure transfer vanishes and the pressure strain is determined from the balance. For the radial Reynolds stress equation and the shear stress equations, both of these terms exist; the pressure transfer term is determined with the relation given by Lumley[19] for homogeneous and nonisotropic turbulent structures that are the most important for transfer:

$$\overline{pu_i}/\rho \approx -\tfrac{1}{5}\overline{q^2 u_i} \tag{2}$$

Note that this term is very small in comparison with pressure strain. However, this result was expected. The large-eddy simulations of Shao et al.[20] of a shearless turbulent mixing layer shows that the constant $\frac{1}{5}$ is an overestimation, and pressure transfer can be easily neglected.

Then, the pressure strain is determined from the balance. The residual errors of the various measured transport terms are the pressure-strain error, because it is balanced from the other terms. This error is estimated around 20% in the inner part of the wake, and decreases to 5% in the outer region.

The axial, radial, and tangential Reynolds stress equations in cylindrical coordinates for an axisymmetric flow, after the boundary-layer approximation, are given by

$$\bar{U}\frac{\partial \overline{u^2}}{\partial x} = -2\overline{uv}\frac{\partial \bar{U}}{\partial r} - \frac{\partial \overline{u^2 v}}{\partial r} - \frac{\overline{u^2 v}}{r} + \frac{2}{\rho}\overline{p\frac{\partial u}{\partial x}} - \frac{2}{3}\varepsilon \tag{3}$$

$$\bar{U}\frac{\partial \overline{v^2}}{\partial x} - \frac{2}{r}\bar{W}\overline{vw} = \frac{2}{r}\bar{W}\overline{vw} - \frac{\partial \overline{v^3}}{\partial r} - \frac{\overline{v^3}}{r} + \frac{2}{r}\overline{vw^2} - \frac{2}{\rho}\frac{\partial \overline{pv}}{\partial r} + \frac{2}{\rho}\overline{p\frac{\partial v}{\partial r}} - \frac{2}{3}\varepsilon \tag{4}$$

$$\bar{U}\frac{\partial \overline{w^2}}{\partial x} + \frac{2}{r}\bar{W}\overline{vw} = -2\overline{vw}\frac{\partial \overline{W}}{\partial r} - \frac{\partial \overline{vw^2}}{\partial r} - \frac{3\overline{vw^2}}{r} + \frac{2}{\rho r}\overline{p\frac{\partial w}{\partial \theta}} - \frac{2}{3}\varepsilon \tag{5}$$

where U, V, and W are the velocity components for the axial, radial, and azimuthal directions, respectively. Note that there is no pressure transfer term in Eqs. (3) and (5).

Afterward, all of the terms for each Reynolds stress transport equation are plotted with their signs. All of the balances are dimensionless, and the radial direction is normalized with the radius of the wake $r*$. We can observe from the balance of the axial equation (Fig. 9) that this flow is mainly dominated by convection, which indicates that the turbulence generated by the propeller is carried downstream in the far wake. Dissipation is continuously decreasing in amplitude from the center to zero in the freestream, while production reaches a maximum around $r/r* \approx 0.6$. The balance of the radial equation (4) shows a convection that is not more important than other transfers (Fig. 10). Turbulent transfer reaches a minimum around $r/r* \approx 0.4$ and a maximum at the boundary of the wake ($r/r* \approx 1.1$) that indicates a change in the energy redistribution between these regions. Other information can be obtained from the balance of Eq. (5), which points out an important amplitude for the convection term, due to the propeller rotation influence (Fig. 11). This term almost equilibrates the sum of pressure strain

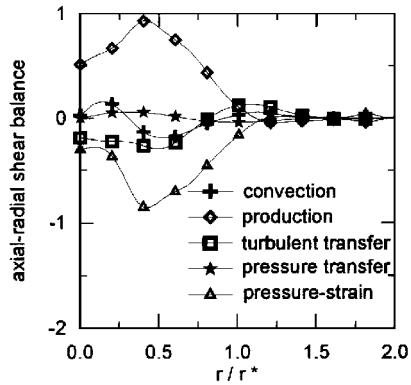

Fig. 12 Axial-radial shear balance.

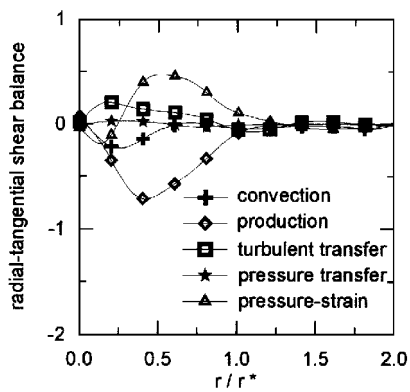

Fig. 13 Radial–tangential shear balance.

and dissipation. A contraction of Eqs. (3–5) brings the kinetic energy balance, in which no pressure-strain term occurs due to continuity (see Refs. 14 and 16).

Similar results are presented for the axial–radial shear equation

$$\bar{U}\frac{\partial \overline{uv}}{\partial x} - \frac{2}{r}\bar{W}\overline{uw} = -\overline{v^2}\frac{\partial \bar{U}}{\partial r} - \frac{\partial \overline{uv^2}}{\partial r} - \frac{\overline{uv^2}}{r} + \frac{\overline{uw^2}}{r} - \frac{1}{\rho}\frac{\partial \overline{pu}}{\partial r} + \frac{1}{\rho}\overline{p\frac{\partial u}{\partial r}} \tag{6}$$

In that case (Fig. 12), an equilibrium between production and pressure strain is established away from the wake axis while convection makes up for turbulent transfer. The axial–tangential shear balance is not significant because of the axisymmetry of the flow.

The distribution for the radial–tangential shear equation is given in Fig. 13:

$$\bar{U}\frac{\partial \overline{vw}}{\partial x} + \frac{\bar{W}}{r}(\overline{v^2} - \overline{w^2}) = -\overline{v^2}\frac{\partial \bar{W}}{\partial r} + \overline{w^2}\frac{\bar{W}}{r} - 2\frac{\overline{v^2 w}}{r} + \frac{\overline{w^3}}{r} - \frac{\partial \overline{v^2 w}}{\partial r} - \frac{1}{\rho}\frac{\partial \overline{pw}}{\partial r} + \frac{1}{\rho r}\overline{p\frac{\partial v}{\partial \theta}} + \frac{1}{\rho}\overline{p\frac{\partial w}{\partial r}} \tag{7}$$

Production is dominant and generated by the mean azimuthal velocity gradient. As for the previous equation, we note an equilibrium between production and pressure strain for $r/r* > 0.3$.

IV. Pressure-Strain Term

We present results of the comparison between the pressure-strain term balanced from the measurements and the corresponding distributions given by classical models. The pressure strain may be divided into three parts:

$$\Pi_{ij} = \Pi^r_{ij} + \Pi^s_{ij} + \Pi^w_{ij} \tag{8}$$

where the first term is denoted the rapid or linear part, the second one is the slow or nonlinear part, and the third one is associated to the wall effects and will be zero in the present case. Afterwards, several models for the rapid part will be tested, together with a single model for the slow part proposed by Rotta.[21] Its expression in Cartesian coordinates is

$$\Pi^s_{ij} = -c_1\varepsilon\left(\frac{\overline{u_i u_j}}{\overline{q^2}} - \frac{2}{3}\delta_{ij}\right) \tag{9}$$

Different values for the constant c_1 are set according to the model used for the rapid part.

Two models, given by Launder et al.,[12] are tested for the rapid part of the pressure strain. The first one is the quasi-isotropic (QI) model

$$\Pi^r_{ij} = -\gamma(P_{ij} - \tfrac{2}{3}P\delta_{ij}) \tag{10}$$

The second one is the isotropic production (IP) model

$$\Pi^r_{ij} = -\frac{c_2+8}{11}\left(P_{ij} - \frac{2}{3}P\delta_{ij}\right) - \frac{8c_2-2}{11}\left(D_{ij} - \frac{2}{3}P\delta_{ij}\right) - \frac{30c_2-2}{55}\left(\frac{\partial \bar{U}_i}{\partial x_j} + \frac{\partial \bar{U}_j}{\partial x_i}\right)\overline{q^2} \tag{11}$$

with

$$P = \frac{P_{kk}}{2} \quad \text{and} \quad D_{ij} = -\left(\overline{u_i u_k}\frac{\partial \bar{U}_k}{\partial x_j} + \overline{u_j u_k}\frac{\partial \bar{U}_k}{\partial x_i}\right)$$

For an axisymmetric flow, the expressions are available in Ref. 22.

For the QI model, the single set $c_1 = 1.5$, $c_2 = 0.4$ is used. Three sets of values are tested for the IP model, $c_1 = 1.5$, $\gamma = 0.6$ (denoted IP 1), which are the first values published in Launder et al.[12]; $c_1 = 1.8$, $\gamma = 0.6$ (denoted IP 2), which were later adjusted by Launder,[23] where the relation $(1-\gamma)/c_1 = 0.23$ is validated; and $c_1 = 3$, $\gamma = 0.3$ (denoted IP 3), which were adjusted for a swirling jet by Gibson and Younis.[10] The last model tested is proposed by Fu et al.[11] for a strongly swirling, recirculating flow. In that expression, the rapid part of pressure strain is calculated not only from production but also from convection:

$$\Pi^r_{ij} = -\gamma(P_{ij} - \tfrac{2}{3}P\delta_{ij} - C_{ij} + \tfrac{1}{3}C\delta_{ij}) \tag{12}$$

with $C = C_{kk}$. The constants c_1 and γ keep the same values as for the IP 1 model. Afterwards, the evolution of the pressure strain given by the several models for the rapid part, in relation with Rotta's model for the slow part, is determined from the measurements of first- and second-order moments of velocity. The gradients that appear in these expressions are calculated in the same way as for the production terms.

We note in Fig. 14, for the pressure-strain term of the axial Reynolds stress equation, that the IP and QI models give the shape of the measured term for $r/r* > 0.5$, but with a lower level than the measured one. There is very little difference between the predictions of IP 1, IP 2, IP 3, and QI. Fu's model is the best one, predicting well the amplitude and the shape of the measured distribution. The pressure-strain term for Eq. (5) is compared with the distributions given by the same models in Fig. 15. It is clear that Fu's model is the only one that is able to predict the evolution of the term in the center of the wake, even if there is a difference of about 45% on the amplitude.

The results for the axial–radial shear are shown in Fig. 16. It can be seen that the pressure-strain term predicted by Fu's model is in very good agreement with data, only the peak level around $r/r* = 0.4$ is slightly underestimated. The IP 1, IP 2, and QI models give similar results, with a lower level than Fu's model, but do not predict well the

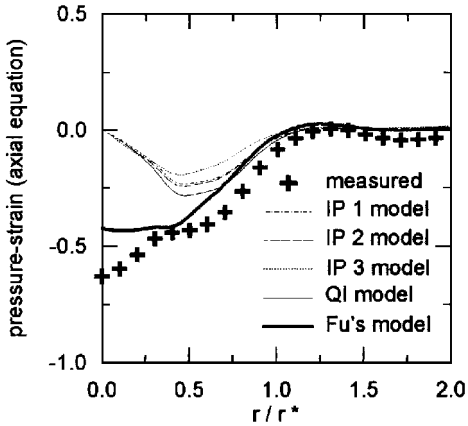

Fig. 14 Comparison between measured and calculated pressure strain for the axial equation.

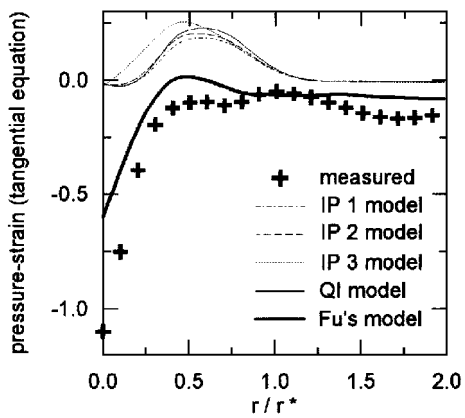

Fig. 15 Comparison between measured and calculated pressure strain for the tangential equation.

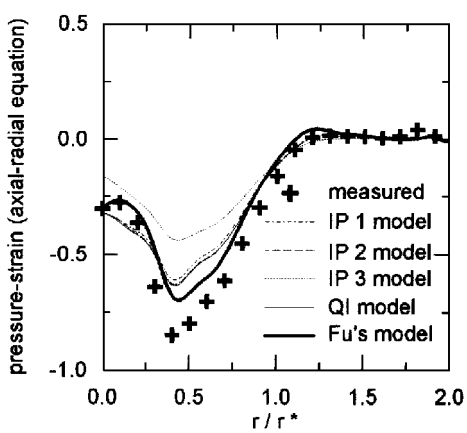

Fig. 16 Comparison between measured and calculated pressure strain for the axial–radial equation.

evolution near the center. The IP 3 model brings the worst behavior, with a peak level about 50% of the experimental value.

The same comments are valid for the radial–tangential shear equation (Fig. 17), where IP 1, IP 2, and QI estimate the measured maximum within about 60% and Fu's model is about 80% of this value, whereas the IP 3 model is almost zero. This surprising difference for this last model calibrated for a swirling jet may lie in the weakness of the swirl and the simple configuration (established jet), whereas Fu's model, calibrated for a strongly swirling recirculating jet, could be applied to many other swirling flows.

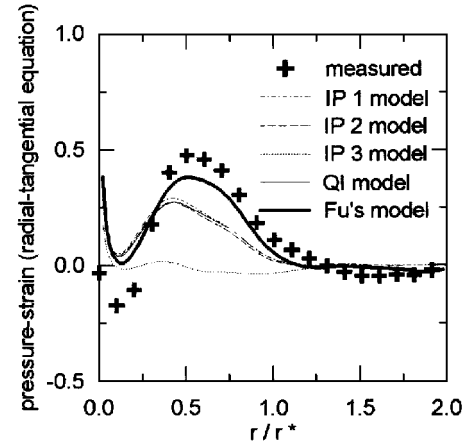

Fig. 17 Comparison between measured and calculated pressure strain for the radial–tangential equation.

V. Conclusion

The different terms of the Reynolds stress transport equations are measured or deduced from the balance, in the momentumless wake of a propeller-driven body. The importance of the convection term in the axial and tangential equations is shown. For the shear equations, a quasiequilibrium between production and pressure strain is established away from the axis of the wake.

Comparisons are made between the experimentally determined evolution of the pressure-strain terms and the corresponding predictions of classical closure models. For any equation, we notice that Fu's model, given for a strongly swirling flow, is very close to the measured terms in the present study. The IP and QI models give a prediction of the shape for pressure strain, away from the center, but underestimate the amplitude. Gibson's model gives an awkward prediction of pressure-strain terms and should not be appropriate for this momentumless rotating wake. This result shows that convection must be an important parameter in the modeling of a momentumless swirling flow.

Acknowledgments

The author wishes to thank G. Comte-Bellot, J. N. Gence, and L. Le Penven for valuable discussions during the course of this work.

References

[1]Lemay, J., Bonnet, J. P., and Delville, J., "Experimental Testing of Diffusion Models in a Manipulated Turbulent Boundary Layer," *AIAA Journal*, Vol. 33, No. 9, 1995, pp. 1597–1603.

[2]Ölçmen, M. S., and Simpson, R. L., "Experimental Transport-Rate Budgets in Complex 3-D Turbulent Flow Near a Wing/Body Junction," AIAA Paper 96-2035, June 1996.

[3]Hussein, H. J., and Martinuzzi, R. J., "Energy Balance for Turbulent Flow Around a Surface Mounted Cube Placed in a Channel," *Physics of Fluids*, Vol. 8, No. 3, 1996, pp. 764–780.

[4]Everitt, K. W., and Robins, A. G., "The Development and Structure of Turbulent Plane Jets," *Journal of Fluid Mechanics*, Vol. 88, Pt. 3, 1978, pp. 563–583.

[5]Panchapakesan, N. R., and Lumley, J. L., "Turbulence Measurements in Axisymmetric Jets of Air and Helium. Part 1. Air Jet, Part 2. Helium Jet," *Journal of Fluid Mechanics*, Vol. 246, 1993, pp. 197–247.

[6]Hussein, J. H., Capp, S. P., and George, W. K., "Velocity Measurements in a High-Reynolds-Number, Momentum-Conserving, Axisymmetric, Turbulent Jet," *Journal of Fluid Mechanics*, Vol. 258, 1994, pp. 31–75.

[7]Aronson, D., and Löfdahl, L., "The Plane Wake of a Cylinder: An Estimate of the Pressure-Strain Rate Tensor," *Physics of Fluids*, Vol. 6, No. 8, 1994, pp. 2716–2721.

[8]Naudascher, E., "Flow in the Wake of Self-Propelled Bodies and Related Sources of Turbulence," *Journal of Fluid Mechanics*, Vol. 22, Pt. 4, 1965, pp. 625–656.

[9]Schetz, J. A., and Jakubowski, A. K., "Experimental Studies of the Turbulent Wake Behind Self-Propelled Slender Bodies," *AIAA Journal*, Vol. 13, No. 12, 1975, pp. 1568–1575.

[10]Gibson, M. M., and Younis, B. A., "Calculation of Swirling Jets with a Reynolds Stress Closure," *Physics of Fluids*, Vol. 29, No. 1, 1986, pp. 38–48.

[11]Fu, S., Launder, B. E., and Leschziner, M. A., "Modelling Strongly Recirculating Jet Flow with Reynolds-Stress Transport Closures," *Proceedings of the 6th Symposium on Turbulent Shear Flows*, Toulouse, France, 1987.

[12]Launder, B. E., Reece, G. J., and Rodi, W., "Progress in the Development of a Reynolds-Stress Turbulence Closure," *Journal of Fluid Mechanics*, Vol. 68, No. 3, 1975, pp. 537–566.

[13]Wyngaard, J. C., and Pao, Y. H., "Some Measurements of the Fine Structure of Large Reynolds Number Turbulence," *Statistical Models and Turbulence*, edited by M. Rosenblatt and C. Van Atta, Springer–Verlag, Berlin, 1971, pp. 384–401.

[14]Faure, T., "Étude expérimentale du sillage turbulent d'un corps à symétrie de révolution autopropulsé par hélice," Ph.D. Thesis, No. 95-01, Laboratoire de Mécanique des Fluides et d'Acoustique, École Centrale de Lyon, Écully, France, Jan. 1995.

[15]Corrsin, S., "Turbulence: Experimental Methods," *Handbuch der Physik*, Vol. 8, Pt. 2, Springer–Verlag, Berlin, 1963, pp. 524–590.

[16]Faure, T., and Robert, G., "Turbulent Kinetic Energy Balance in the Wake of a Self-Propelled Body," *Experiments in Fluids*, Vol. 21, No. 4, 1996, pp. 268–274.

[17]Browne, L. W. B., Antonia, R. A., and Shah, D. A., "Turbulent Energy Dissipation in a Wake," *Journal of Fluid Mechanics*, Vol. 179, 1987, pp. 307–326.

[18]Faure, T., and Robert, G., "Bilans de tension de Reynolds dans un sillage de traînée et dans un sillage de corps autopropulsé par une hélice," *Comptes-Rendus de l' Académie des Sciences*, Paris, Vol. 321, No. 11, Série II b, 1995, pp. 455–461.

[19]Lumley, J. L., "Computational Modeling of Turbulent Flows," *Advances in Applied Mechanics*, edited by C. S. Yih, Vol. 18, Academic, New York, 1978, pp. 123–174.

[20]Shao, L., Le Penven, L., and Bertoglio, J. P., "Study of the Modelling of the Transport Terms in One-Point Closures Using Large Eddy Simulation of Turbulence," *Engineering Turbulence Modelling and Experiments*, edited by W. Rodi and E. N. Ganic, Elsevier Science, New York, 1990, pp. 83–92.

[21]Rotta, J. C., "Statistiche Theorie nichthomogener Turbulenz," *Zeitschrift für Physik*, Vol. 129, 1951, pp. 547–572.

[22]Launder, B. E., and Morse, A., "Numerical Prediction of Axisymmetric Free Shear Flows with a Reynolds Stress Closure," *Turbulent Shear Flows I*, Springer–Verlag, Berlin, 1979, pp. 279–294.

[23]Launder, B. E., "Second-Moment Closure and its Use in Modelling Turbulent Industrial Flows," *International Journal for Numerical Methods in Fluids*, Vol. 9, 1989, pp. 963–985.